

# International Workshop on Computational Nanotechnology

## 3D Monte Carlo simulations of strained Si GAA nanowire FETs with different channel orientations

M A Elmessary<sup>1,2</sup>, D Nagy<sup>3</sup>, M Aldegunde<sup>4</sup>, A J García-Loureiro<sup>3</sup> and K Kalna<sup>1</sup>

<sup>1</sup>Swansea University, UK, <sup>2</sup>Mansoura University, Egypt, <sup>3</sup>Universidade de Santiago de Compostela, Spain, <sup>4</sup>University of Notre Dame, USA

GAA NW FETs are considered to be the most promising candidates for sub-10 nm digital technology suitable for future CMOS integration due to their superior electrostatics, immunity to short channel effects and large on-current [1]. Strain technology can enhance the drain current [2] but the effectiveness of strain can be reduced due to the pre-existing quantum confinement induced valley splitting [3].

In this work, we study the effects of uniaxial tensile strain in nanoscale Si GAA NW FETs affected by surface and channel orientation with our in-house 3D Finite Element (FE) Monte Carlo (MC) toolbox which uses the calibration-free Schrödinger Equation based Quantum Corrections (SEQC) [4–6] allowing to account for exact nanoscale geometry and thus confinement. The 3D FE mesh contains predefined 2D planes perpendicular to transport direction to solve 2D Schrödinger Eq. separately for the three/six  $\Delta$  valleys:

$$-\frac{\hbar^2}{2} \nabla_{\perp} \cdot [(\mathbf{m}^*)^{-1} \cdot \nabla_{\perp} \psi(y, z)] + U(y, z) \psi(y, z) = E \psi(y, z),$$

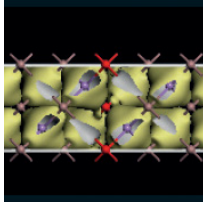
where  $(\mathbf{m}^*)^{-1}$  is the inverse effective mass tensor listed in Table 1,  $U(y, z) = -[qV(y, z) + \chi(y, z)]$  is the potential energy,  $\chi(y, z)$  is the electron affinity,  $\psi(y, z)$  is the wavefunction penetrating into oxide, and  $E$  is the energy [5].

Fig. 1 shows 6 Si  $\Delta$  valleys within confinement cross-section along the transport direction. The strain is modeled by shifting the Si valley by  $\Delta E_C$  according to the strain type and strength (Table 2) [8]. For the uniaxial  $\langle 110 \rangle$  strain, the transverse effective masses in  $\Delta 3$  valley split due to a band-structure warping resulting in a lighter  $m_t^{transport}$  and a heavier  $m_t^{perpendicular}$  [8].

The GAA NW FET has an elliptical cross-section ( $R=5.7/7.17$  nm) and a gate length of 10 nm with EOT=0.8 nm (Fig. 2). We simulate  $\langle 100 \rangle$  and  $\langle 110 \rangle$  channel orientations and two types of tensile strain: uniaxial  $\langle 100 \rangle$  and uniaxial  $\langle 110 \rangle$  with strengths of 0.5%, 0.7% and 1.0%. To show the effect of confinement on strain, the 10 nm gate NW is compared to a bigger device with an elliptical cross-section ( $R=11.3/14.22$  nm) and a gate length of 22 nm with EOT=1.5 nm [1]. The MC toolbox was verified against experimental data for the 22 nm GAA NW with excellent agreement [1, 7].

Fig. 3 shows ID-VG characteristics at  $V_D=0.7$  V for the 10 nm gate length NW in the  $\langle 100 \rangle$  channel orientation under three uniaxial  $\langle 100 \rangle$  strengths of strain delivering increase in the drive-current by 6%, 6.9% and 7.3%, respectively. The sub-threshold slope exhibits a small deterioration under the increasing strain strength. Fig. 4 plots the 3  $\Delta$  valleys contributions to the current in the  $\langle 100 \rangle$  device under uniaxial  $\langle 100 \rangle$  strain with indicated strengths. In this case,  $\Delta 1$  valley is shifted up reducing its contribution to the drain current because it has the largest effective transport mass ( $m_t$ ) (see Table 2).  $\Delta 2$  and  $\Delta 3$  valleys (Table 2) are shifted down increasing their contributions to the drain current because of a smaller effective transport mass ( $m_t$ ).

Since a larger confinement (perpendicular-to-transport) mass results in a lower bound state, the  $\Delta 3$  with a larger confinement effective mass ( $m_t$ ) contributes more to the current than  $\Delta 2$ . The reduction in the strain effectiveness caused by the quantum confinement due to the pre-existing valley splitting is seen in the less confined 22 nm device (Fig. 5). The 0.5/0.7/1.0% uniaxial  $\langle 100 \rangle$  strain increases the drive current (at



# International Workshop on Computational Nanotechnology

$V_{DD}=1.3$  V) in the 22 nm gate length NW FET by 16.6/19.3/21.4% compared to only 6/6.9/7.3% for the 10 nm gate length device.

Fig. 6 shows  $I_D-V_G$  characteristics for the 10 nm gate length NW FET with a  $\langle 100 \rangle$  channel orientation at  $V_D=0.7$  V under uniaxial  $\langle 100 \rangle$  strain. In the  $\langle 100 \rangle$  orientation, a transformation of coordinates is performed since the ellipsoid principal axes are not aligned with the device coordinate system [4, 9]. Without applying any strain, the  $\langle 100 \rangle$  channel device delivers more current (20.4%) than the  $\langle 110 \rangle$  channel device due to enhanced mobility (lighter effective transport mass). When applying uniaxial  $\langle 100 \rangle$  strain, the drive-current at  $V_{DD}=1.0$  V increases by 4.2%, 4.8%, and 3.3% at increasing strain strengths, respectively. The drive-current drop at 1.0% strain is due to the swap of valley contributions to the current with increasing strain. Although  $\Delta 3$  contributes more to the current than  $\Delta 1$  and  $\Delta 2$ , it has smaller increment from 1.0% strain than 0.7% strain while the  $\Delta 1$  and  $\Delta 2$  valleys reduce the current more at the 1.0% strain (see Fig. 7). For the  $\langle 110 \rangle$  side-walls, the  $\Delta 3$  has a smaller confinement mass ( $0.19m_0$ ) than that of  $\Delta 1$  and  $\Delta 2$  ( $0.315m_0$ ). However, the  $\Delta 1$  and  $\Delta 2$  have a larger confinement mass resulting in a confinement of carriers to appear closer to the interface charge. To see the effect of confinement, Fig. 8 shows a comparison for the less-confined 22 nm gate length NW in which the 0.5/0.7/1.0% uniaxial  $\langle 110 \rangle$  strain increases the drive current (at  $V_{DD}=1.0$  V) by 11.6/12.7/7.6% compared to only 4.2/4.8/3.3% in the 10 nm gate device.

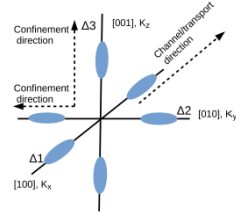


Fig. 1: Schematic of six Si valleys along a confinement plane. The transport direction is along the x-axis.

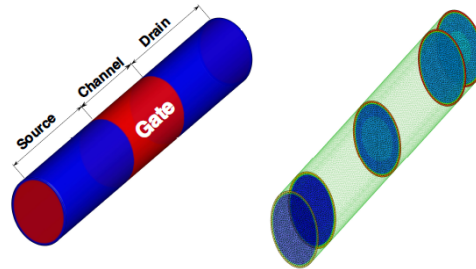


Fig. 2: Schematic of the investigated  $n$ -channel Si GAA nanowire FET (left) and the device mesh with sample of the 2D slices for the Schrödinger solver (right).

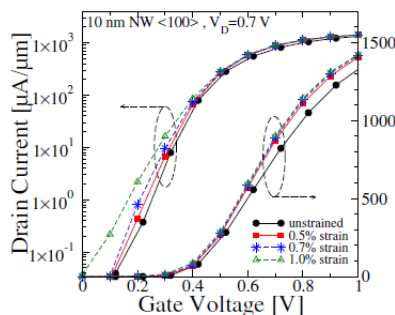


Fig. 3:  $I_D-V_G$  characteristics at  $V_D=0.7$  V for the 10 nm gate length GAA-NW with  $\langle 100 \rangle$  channel orientation under different uniaxial  $\langle 100 \rangle$  strain strengths.

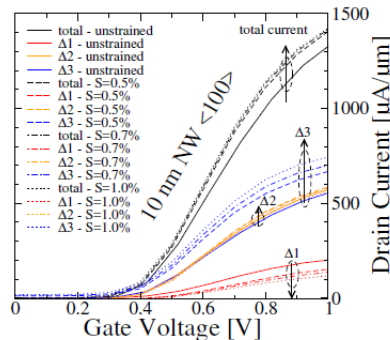


Fig. 4: Valley contributions to the current at  $V_D=0.7$  V for the 10 nm gate length GAA-NW with  $\langle 100 \rangle$  channel orientation under different uniaxial  $\langle 100 \rangle$  strain strengths.

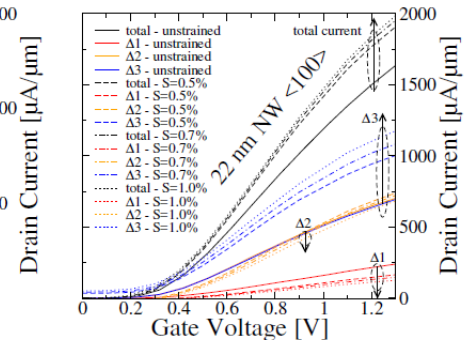
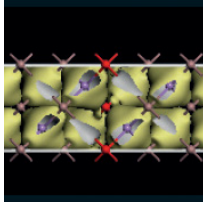


Fig. 5: Valley contributions to the current at  $V_D=1.0$  V for the 22 nm gate length GAA-NW with  $\langle 100 \rangle$  channel orientation under different uniaxial  $\langle 100 \rangle$  strain strengths.



# International Workshop on Computational Nanotechnology

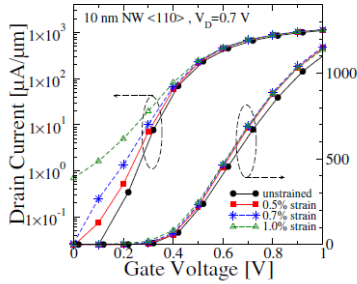


Fig. 6:  $I_D$ - $V_G$  characteristics at  $V_D=0.7$  V for the 10 nm gate length GAA-NW with  $\langle 110 \rangle$  channel orientation under different uniaxial  $\langle 110 \rangle$  strain strengths.

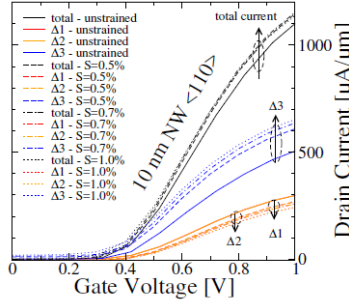


Fig. 7: Valley contributions to the current at  $V_D=0.7$  V for the 10 nm gate length GAA-NW with  $\langle 110 \rangle$  channel orientation under different uniaxial  $\langle 110 \rangle$  strain strengths.

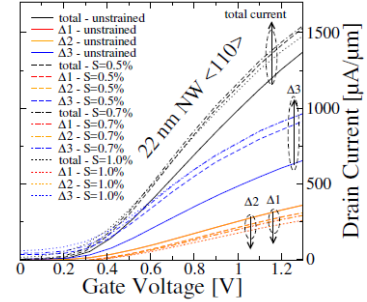


Fig. 8: Valley contributions to the current at  $V_D=1.0$  V for the 22 nm gate length GAA-NW with  $\langle 110 \rangle$  channel orientation under different uniaxial  $\langle 110 \rangle$  strain strengths.

Orientation	Valley	$1/m_{xy}^*$	$1/m_{zz}^*$	$m_{\Gamma}^*$
$\langle 100 \rangle$	$\Delta 1$	$1/m_t$	$1/m_t$	$m_t$
$\langle 100 \rangle$	$\Delta 2$	$1/m_t$	$1/m_t$	$m_t$
$\langle 100 \rangle$	$\Delta 3$	$1/m_t$	$1/m_t$	$m_t$
$\langle 110 \rangle$	$\Delta 1$	$(m_t + m_l)/(2m_t m_l)$	$1/m_t$	$(m_t + m_l)/2$
$\langle 110 \rangle$	$\Delta 2$	$(m_t + m_l)/(2m_t m_l)$	$1/m_t$	$(m_t + m_l)/2$
$\langle 110 \rangle$	$\Delta 3$	$1/m_t$	$1/m_l$	$m_t$

Table 1: Effective-mass tensor and effective transport mass of  $\Delta$  valleys for  $\langle 100 \rangle$  and  $\langle 110 \rangle$  channel orientations where  $1/m_{yz}^*=0$  and degeneracy = 2.

Strain type strain strength	Uniaxial $\langle 100 \rangle$ strain			Uniaxial $\langle 110 \rangle$ strain		
	0.5%	0.7%	1.0%	0.5%	0.7%	1.0%
$\Delta 1$	+0.03eV	+0.042eV	+0.06eV	-0.01eV	-0.014eV	-0.02eV
$\Delta 2$	-0.045eV	-0.063eV	-0.09eV	-0.01eV	-0.014eV	-0.02eV
$\Delta 3$	-0.045eV	-0.063eV	-0.09eV	-0.065eV	-0.091eV	-0.13eV

Table 2: Valley-edge shifts for each valley with different types and strengths of tensile strain [8].

- [1] S. Bangsaruntip et al., *IEDM Tech. Dig.*, pp. 526-529, 2013.
- [2] Keng-Ming Liu et al., *IEEE TED*, vol. 58, no. 10, 2011.
- [3] M. V. Fischetti et al., *J. Appl. Phys.*, vol. 92, no. 12, pp. 7320-7324, 2002.
- [4] M. A. Elmessary et al., *IEEE TED*, vol. 63, no. 3, pp. 933-939, 2016.
- [5] J. Lindberg et al., *IEEE TED*, pp. 423-429, 2014.
- [6] M. Aldegunde et al., *IEEE TED*, pp. 1561-1567, 2013.
- [7] M. A. Elmessary et al., *Solid-St. Electron.*, vol. 128, pp. 17-24, 2017.
- [8] K. Uchida et al., *IEDM Tech. Dig.*, pp. 129-132, 2005.
- [9] A. Rahman et al., *J. Appl. Phys.*, vol. 97, no. 5, pp. 053702, 2005.